Cell Reports
Physical Science

Article

Weldable graphene foams for wide-range thermal switches

Graphical abstract

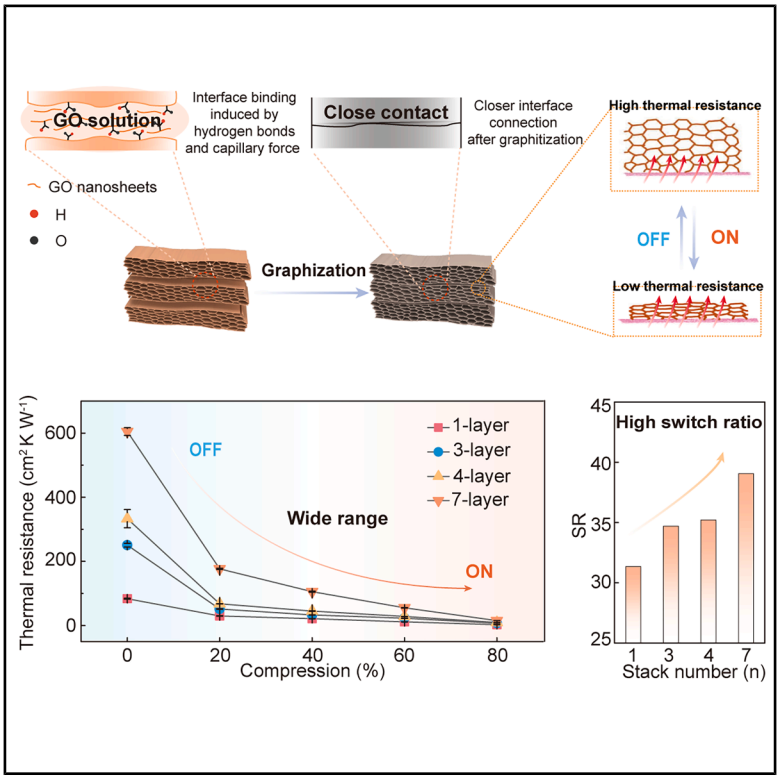

Highlights

- Scalable welding of elastic graphene foams is achieved
- The thermal resistance of graphene foams exhibits a wide range of 15.49–604.85 cm^2 K W^{-1}
- Graphene foams demonstrate superior performance in dynamic thermal management

Authors

Shiya Cao, Huaqiang Fu, Pengfei Chen, ..., Chao Tian, Lun Li, Daping He

Correspondence

fuhuaqiang@whut.edu.cn (H.F.), llunhy@whut.edu.cn (L.L.), hedaping@whut.edu.cn (D.H.)

In brief

Cao et al. report a multilayer welding strategy for elastic graphene foam. The obtained multilayer graphene foams exhibit a wide range of thermal resistance adjustment and a high switch ratio within the elastic range, showing great promise in dynamic thermal management applications.

Cao et al., 2025, Cell Reports Physical Science 6, 102599
May 21, 2025
https://doi.org/10.1016/j.xcrp.2025.102599

CellPress

Cell Reports
Physical Science

CellPress
OPEN ACCESS

Article

Weldable graphene foams for wide-range thermal switches

Shiya Cao,[1,2,5] Huaqiang Fu,[1,2,5,*] Pengfei Chen,[1,2] Hao Feng,[1,2] Ziran Zhang,[2,3] Ziqi Lin,[2,3] Zhe Wang,[2,4] Wei Qian,[2] Chao Tian,[1,2] Lun Li,[2,*] and Daping He[1,2,6,*]

[1]School of Materials Science and Engineering, Wuhan University of Technology, Wuhan 430070, China
[2]Hubei Engineering Research Center of RF-Microwave Technology and Application, School of Physics and Mechanics, Wuhan University of Technology, Wuhan 430070, China
[3]School of Materials and Microelectronics, Wuhan University of Technology, Wuhan 430070, China
[4]State Key Laboratory of Advanced Technology for Materials Synthesis and Processing, Wuhan University of Technology, Wuhan 430070, China
[5]These authors contributed equally
[6]Lead contact
*Correspondence: fuhuaqiang@whut.edu.cn (H.F.), llunhy@whut.edu.cn (L.L.), hedaping@whut.edu.cn (D.H.)
https://doi.org/10.1016/j.xcrp.2025.102599

SUMMARY

Dynamic thermal regulation has become the pivotal issue for future electronics thermal management. Porous elastic materials have been widely developed as smart thermal switches, exhibiting compression-induced tunable heat transfer behavior. However, such tunability is severely restricted by the limited out-of-plane macroscale. Herein, we report a multilayer welding strategy for fabricating graphene foam (GF) thermal switches with wide tuning ranges (TRs) and high switch ratios (SRs). Infinitely expanding the out-of-plane size is realized by constructing a reliable welding interface, leveraging the capillary force and hydrogen bonding within graphene oxide foam. After graphitization, the obtained multilayer GFs (M-GFs) demonstrate excellent elasticity and wide thermal resistance TRs. Specifically, the 7-layer GFs demonstrate an ultra-wide TR of thermal resistance (15.49–604.85 cm^2 K W^{-1}) and a much-improved SR (39.0) within the elastic range. When applied to lithium-ion battery thermal management, M-GFs ensure safe temperature and maintain discharge capacity, showing great potential in dynamic thermal management.

INTRODUCTION

The application of electrical equipment in complex environments requires the development of dynamic thermal management technologies, aiming to enhance performance, extend lifespan, and ensure high safety.[1–8] Especially when confronted with the vastly different thermal management requirements in high- and low-temperature environments, the single functionality of traditional heat dissipation or insulation material is insufficient to satisfy the complex operational conditions.[9,10] Thermal switches capable of intelligently tunable heat transfer behavior show potential for addressing dynamic thermal management.[1,11,12] However, traditional thermal switches merely show binary operational modes (on/off),[13–15] which cannot adapt to the dynamic environment. Existing research on optimizing thermal switches, such as electric/magnetic field regulation of conductive particles[16–19] and phase-change materials,[20–23] are still limited by finite switch ratios (SRs) and discrete changes in thermal conductivity.

Recent advancements have focused on the development of strain-responsive thermal switches utilizing porous elastic materials, which exhibit continuous, reversible, and compression-tunable heat transfer properties.[24–28] Despite their potential, these materials are often hindered by a narrow tuning range (TR) and a relatively low SR. Graphene, renowned for its exceptional thermal conductivity and mechanical properties,[29] emerges as an ideal candidate for constructing high-performance strain-responsive thermal switches. For example, Ruan et al. reported a compressible graphene foam (GF) thermal switch with a thermal SR of 8 (223.7–27.6 cm^2 K W^{-1}).[30] Zhang et al. synthesized a graphene aerogel via a hydrothermal method for battery thermal management, demonstrating a TR of thermal resistance from 229 to 69.5 cm^2 K W^{-1}.[31] However, due to the limitations in the macroscopic dimensions of GF, as well as inevitable issues including poor interfacial bonding[32] and internal structural inhomogeneity when assembled into large-scale structures, it remains challenging to develop GF thermal switches with wide TRs and high SRs.

In this study, a multilayer welding strategy is applied to fabricate GF thermal switches with a wide TR and high SR. By employing the bubble templating technique, the stable growth of bubbles was precisely controlled within the dispersion medium, enabling the synthesis of highly porous graphene oxide foam (GOF) with a three-dimensional (3D) structure. After high-temperature reduction, the single-layer GF (S-GF) exhibits exceptional elasticity, fatigue resistance, and a range of thermal

Please cite this article in press as: Cao et al., Weldable graphene foams for wide-range thermal switches, Cell Reports Physical Science (2025), https://doi.org/10.1016/j.xcrp.2025.102599

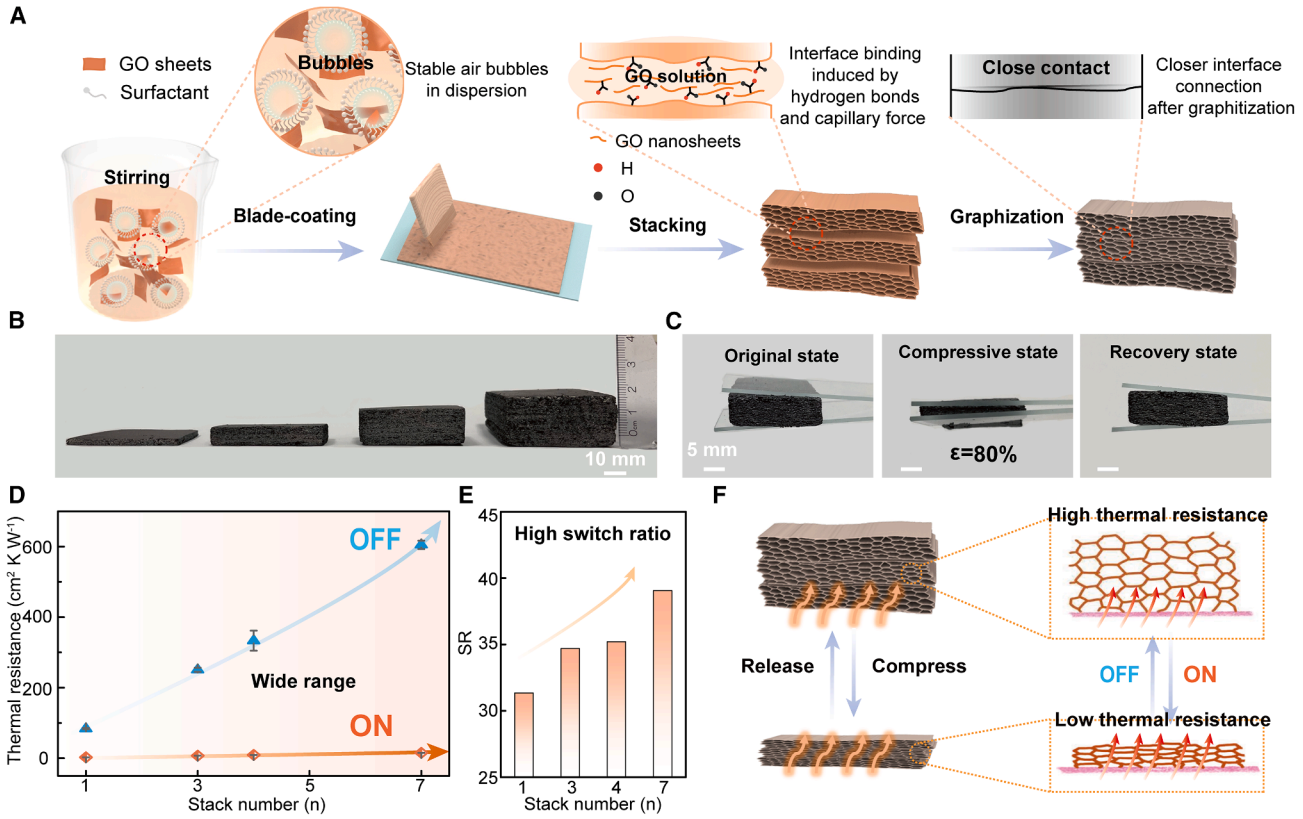

Figure 1. Fabrication and application of GF as a thermal switch

(A) Fabrication process of GF.

(B) Photographs of GF with different stacking thicknesses. The scale bar represents 10 mm.

(C) Photographs of M-GFs under original, compressive (ε = 80%), and recovery states, respectively. The scale bar represents 5 mm.

(D and E) Schematic diagram illustrating the wide-range adjustable thermal resistance and high switch ratio achieved by GF with different stack numbers.

(F) Schematic diagram of M-GFs applied to thermal switch.

resistances from 83.83 to 2.67 cm^2 K W^{-1}. To further broaden the TR of thermal resistance, the multilayer assembly of GOF was achieved by utilizing an aqueous GO solution as an interfacial binder. Multilayer GFs (M-GFs) were subsequently obtained after graphitization, which exhibit ultra-wide-tunable, macroscale, well-welded interfaces; adjustable thermal properties; and scalable mechanical and thermal performances. Specifically, within the elastic range, the 7-layer GFs demonstrate a breakthrough of ultra-wide TRs of thermal resistance (15.49–604.85 cm^2 K W^{-1}) and an improved SR (39.0).

RESULTS AND DISCUSSION

Synthesis and characterization of GF

Initially, foamed GO slurry was prepared by introducing surfactant into GO aqueous slurry under vigorous mechanical stirring. The detailed characterization of the GO slurry is shown in Figures S1 and S2. The surface activity of the surfactant effectively facilitated the uniform generation and stable existence of bubbles between the GO sheets, with a controlled foaming ratio of approximately 2.0 times (Figures 1A and S3). Optical microscopic images revealed that the bubble diameters in the foamed GO slurry ranged from 50 to 100 μm (Figure S4). The introduction of these bubbles not only enriched the microstructure of the slurry but also laid the foundation for the formation of subsequent 3D structures. The foamed GO slurry could be shaped into a 3D GOF through a one-step process of flat coating and subsequent drying under natural conditions (Figure S5). Specifically, GOF was fabricated by drying it at room temperature without the incorporation of a reduction step. Consequently, the surface of GOF is abundant with oxygen-containing functional groups, enabling the direct utilization of GO aqueous solution as an interfacial adhesive for the layer-by-layer stacking construction of single-layer GOF. During the stacking and subsequent drying, the formation of hydrogen bonds and capillary forces further enhances the cohesive adhesion between different interfaces, thereby ensuring the stability and integrity of the GOF bulk. During high-temperature graphitization, the graphene lattices at the interfaces undergo further rearrangement, resulting in an enhancement of interfacial strength. These series of procedures ultimately achieve the preparation of a weldable GF with adjustable thickness. Raman analysis of GOF and GF (Figure S6) revealed that the D band (≈1,340 cm^{-1}) nearly vanished in GF, confirming a significant improvement in the crystallinity of the

Please cite this article in press as: Cao et al., Weldable graphene foams for wide-range thermal switches, Cell Reports Physical Science (2025), https://doi.org/10.1016/j.xcrp.2025.102599

GOF after annealing. The reduction in defect-induced phonon scattering notably improved the thermal conductivity of GF.[33] Simultaneously, the X-ray diffraction (XRD) pattern exhibits sharp (002) and (004) peaks at 26.6° and 54.7°, respectively, further confirming the formation of graphitic structures and the ordered stacking of graphene layers within GF.[34] The porous structure of GOF remains intact after graphitization (Figure S7), thereby endowing GF with low density, high porosity, and exceptional resilience (Table S1). By precisely controlling the number of stacked layers, customized adjustment of the thickness of GF (Figure 1B) can be achieved. M-GFs exhibit good elasticity (Figure 1C), allowing the flexible adjustment of the thermal resistance range of M-GFs in both its on and off states within a broad range by tuning the number of stacked layers and compression (Figure 1D). As the number of stacked layers increases, the interfaces exhibit increasingly tight bonding, accompanied by an increase in thermally conductive solid-phase components during compression and a decrease in contact thermal resistance. Such modulation leads to a continuous rise in thermal resistance when the thermal switch is in the off state while maintaining an extremely low level in the on state, thereby achieving a high thermal SR (Figure 1E). This unique stacking strategy, combined with the porous elastic structure, enables M-GFs to continuously and broadly control the heat flow transmittance by simply adjusting the degree of compression, demonstrating its enormous application potential as a dynamic thermal management material (Figure 1F).

Mechanical and thermal properties of S-GF

Distinct from conventional freeze-drying methods that rely on the disordered growth of ice crystals to produce 3D GF with random structures, here, stable bubble templates were introduced *in situ* within the precursor GO dispersion by regulating its concentration. This results in the uniform and stable presence and growth of bubbles (Figure 2A), thereby imparting GF with an abundant and ordered pore structure. As illustrated in Figure 2B, the internal pressure within smaller bubble A (r_A) is higher than that of larger bubble B (r_B). With the continuous evolution of the gas-liquid interface, gases between bubbles tend to diffuse from smaller to adjacent larger bubbles under the action of Laplace pressure differences. P_L is the liquid pressure. This dynamic process leads to the shrinkage of smaller bubbles, while larger bubbles expand by engulfing smaller ones until rupturing, which could induce inhomogeneity in the porous structure and reduce porosity. Hence, the effective suppression of the Ostwald ripening phenomenon is crucial for the fabrication of GF that possesses uniform pore structures and high porosity. According to theoretical and experimental research,[35] once the bubbles are stably generated, the subsequent growth of bubbles and the ultimate morphology of the porous structure are significantly influenced by the concentration and viscosity of the GO dispersion. SDS was selected as the surfactant[36] to ensure stable bubble generation in the GO dispersion by studying the bubble growth behavior of GO slurry under the action of different surfactants (Figure S8; Note S1). Bubble templates can be uniformly dispersed in the GO dispersion only within an appropriate concentration range, forming a rich pore structure, thereby imparting excellent mechanical properties to the GF. As shown in Figures S9 and S10, at low GO concentrations, abundant bubbles are rapidly generated; however, the low system viscosity reduces bubble growth resistance, causing small bubbles to dissipate quickly via Ostwald ripening while larger bubbles continue to grow. This results in an uneven pore size distribution upon drying. Conversely, excessively high GO concentrations increase viscosity, which restricts both the dispersion and initial growth of bubbles and subsequently impedes their further enlargement, thereby affecting the uniformity of the graphitized pore structure (Figure S11). In Figure 2A, at an optimal concentration (25 mg mL^{-1}), bubbles gradually grow over time, while the number of nucleation sites remains relatively stable (Figure S12), preserving more small bubbles and the formation of a uniform pore structure with interwoven large and small bubbles that provide abundant pore units for S-GF, thereby significantly enhancing the mechanical integrity of the material. (Figures 2C and 2D). This unique geometric configuration effectively cushions external forces and rapidly restores the initial shape, determining the high recoverability of the foam under large compressive strains (Figures S13 and S14; Note S2).

The cells are organized in a honeycomb-like configuration to maximize the elasticity of GF, which is essential for strain-responsive thermal switches. Simultaneously, the cell walls are stacked with thicker graphene sheets, which provide enhanced mechanical strength and structural integrity.[37] To validate the mechanical properties of S-GF, uniaxial compression tests were conducted under ambient conditions. S-GF exhibits outstanding elasticity under large compressive strain, achieving a recoverable strain of up to 80% (Figures 2E and S15). Moreover, in Figure 2F, the stress-strain curve obtained during various strain loading processes conforms to the characteristics of the most resilient materials[38]: (1) low strain ($\varepsilon < 15\%$) exhibited a typical linear elastic region, where stress increases linearly with strain, reflecting the material's good initial stiffness. (2) A plateau region of $15\% < \varepsilon < 50\%$ related to the elastic buckling of porous materials demonstrated its superior deformation absorption capability. (3) A high-strain densification region appeared at $\varepsilon > 50\%$, and there was a sharp increase in stress, corresponding to the densification process of pores, further proving the structural stability of S-GF under high-strain conditions. The pressure required to achieve the maximum strain is merely 35.4 kPa. Such a low-pressure requirement significantly facilitates the intimate contact between S-GF and the heating element or heat dissipation device, effectively reducing the contact thermal resistance. Furthermore, S-GF also exhibits impressive fatigue resistance, nearly recovering its original shape after 500 consecutive compression cycles (Figure 2G). The structural integrity of S-GF is well preserved even after the process (Figure S16). The energy loss coefficient rapidly stabilizes after initial fluctuations, and the maximum stress value of S-GF remains at 84.67% of its original value even after 500 compression cycles, indicating the structural stability and reliability of S-GF for long-term use.

The remarkable elasticity and high porosity endow S-GF with the ability to continuously and reversibly adjust thermal resistance in response to strain variations. Thermal resistance, as a crucial parameter for measuring heat transfer obstacles, directly reflects the efficiency and capability of materials or structures in

CellPress
OPEN ACCESS

Cell Reports
Physical Science
Article

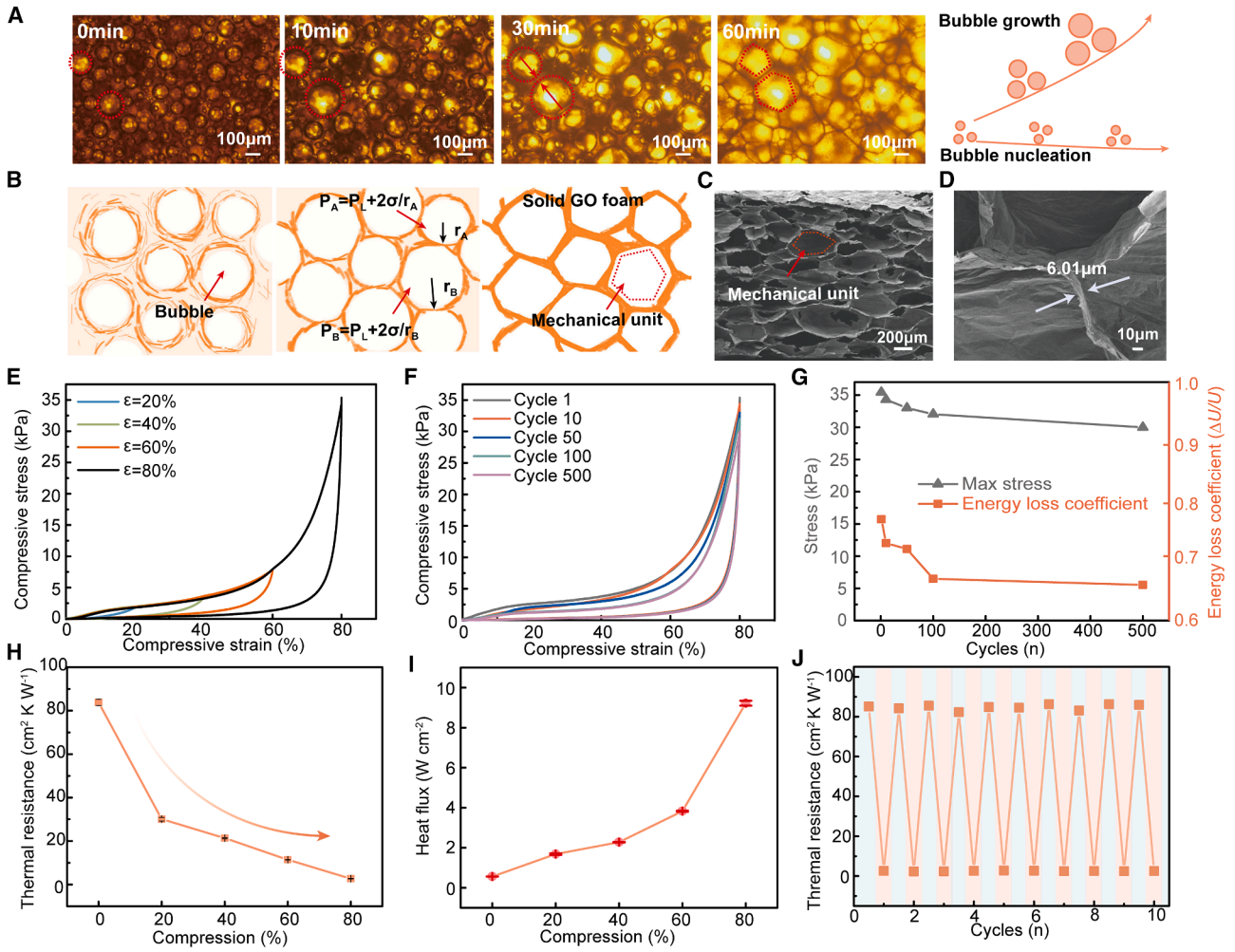

Figure 2. Structural and mechanical-thermal properties of S-GF

(A) Optical microscope images of bubble nucleation (remaining almost the same number) and bubble growth (bubble expanding) and their corresponding schematic diagrams.

(B) Schematic diagram of the bubble growth process.

(C) Cross-sectional SEM image of S-GF.

(D) Enlarged SEM image of the pore wall of S-GF.

(E) Compressive σ versus ε curves of S-GF under different compressive loadings, with ε at 20%, 40%, 60%, and 80%, respectively.

(F) 500-cycle fatigue tests with a compressive strain of 80%.

(G) Maximum stress energy loss coefficient and max stress versus compression 500 cycles.

(H and I) Thermal resistance and heat flux of the S-GF with different compression rates.

(J) Cyclicity of off and on states of thermal resistance for the S-GF.

the process of heat transfer. Figure 2H clearly reveals the unconventional thermal regulation mechanism of the S-GF, which transcends the binary on/off state of traditional thermal switches. Instead, precise control of thermal resistance is achieved by continuously adjusting the compression degree, thereby endowing the device with dynamic adaptability and regulatory capabilities in the heat transfer process. The specific thermal resistance test principle is shown in Figure S17. Specifically, as the degree of compression gradually increases, the thermal resistance of the S-GF exhibits a pronounced downward trend within the elastic strain range (0%–80%), significantly decreasing from an initial value of 83.83 to 2.67 cm^2 K W^{-1}. This alteration signifies a substantial reduction in the obstacles to heat flow within the material, with a corresponding marked increase in the heat flux through S-GF as the degree of compression intensifies (Figure 2I). This could be attributed to the compression-induced decrease in porosity, which significantly enhances the density of thermal conduction pathways within S-GF, thereby accelerating the transfer of heat along the skeletal structure of S-GF and substantially elevating its overall thermal conductivity. The results of the cyclic compression tests depicted in Figure 2J indicate that even after undergoing ten cycles of repeated compression, the S-GF maintains stable thermal switch performance without exhibiting any discernible signs of performance degradation. The

Please cite this article in press as: Cao et al., Weldable graphene foams for wide-range thermal switches, Cell Reports Physical Science (2025), https://doi.org/10.1016/j.xcrp.2025.102599

specific thermal resistance data are shown in Table S2. To validate the thermal resistance stability of S-GF under humid and pressurized conditions, the thermal resistance was continuously monitored long term at a relative humidity (RH) of 75% and a constant pressure of 35.4 kPa (ε = 80%). The thermal resistance remained stable, demonstrating the excellent thermal stability of S-GF in both humid and pressurized environments (Figure S18).

Properties of M-GFs

Due to the ubiquitous mismatch issue, direct solid-state assembly of GO foams frequently encounters challenges in achieving satisfactory structural integrity.[39] Such issues were addressed in the work by drying the foamed GO slurry at room temperature and directly introducing a GO aqueous solution as an interfacial binder. These GO architectures possess substantial hydrogen bond networks, which are composed of oxygen-containing functional groups on individual GO sheets and water molecules between the layers, facilitating interface healing and rearrangement. As shown in Figures S19 and S20, X-ray photoelectron spectroscopy (XPS) analysis of the GOF surface confirms the presence of abundant oxygen-containing functional groups. Fourier transform infrared spectroscopy (FTIR spectroscopy) analysis was performed on the GOF and its stacked interfaces before and after drying. The results reveal that the dried GOF has trouble forming hydrogen bonds due to the absence of water molecules. However, with the insertion of water molecules, hydrogen bonds are re-established. Subsequently, the evaporation of water molecules restores the infrared spectrum of the GOF interface to its initial state. This indicates that the hydrogen bonds at the welded interface of GOF undergo reconstruction, leading to interfacial healing.[40–43] During the subsequent air-drying process, narrow gaps between GOFs induce capillary forces, prompting interfacial contraction. In the graphitization stage, lattice rearrangement occurs at the graphene interfaces, resulting in tighter interfacial bonding (Figure 3A).[44] Scanning electron microscopy (SEM) images (Figures 3B and 3C) reveal that prior to graphitization, there exist minute interfacial gaps at the junctions of the GOF film. However, after graphitization, these interfaces are tightly bonded together. 3-layer GFs (~133 mg) can even resist a weight of 100 g without any fracture occurring (Figure 3D). It is noteworthy that as the number of stacked layers increases, the thickness of the GF exhibits a linear growth trend (Figure 3E; Table S3), indicating that the adoption of the stacking strategy has not led to the collapse of the foamed structure. When the 3-layer GFs are disrupted by tensile force, the fracture surface does not propagate along the interfaces (Figure 3F). Further SEM observation of the fracture surface (Figure 3G) reveals that the fracture occurs along the internal porous structure, providing robust evidence for the existence of strong adhesion effects between the graphene interfaces. This strong adhesion is mainly attributed to the following aspects. Firstly, during the air-drying process, the hydrogen bond self-healing and capillary forces of the stacked GOF play a crucial role. Secondly, during the graphitization process, the rearrangement of the graphene lattice contributes to the strong adhesion. The mechanical compression characteristics of the 3-layer GFs were also investigated, and the results are presented in Figure S21 and Video S1. Notably, the 3-layer GFs still exhibit excellent resilience within an 80% strain range, indicating that the M-GFs retain the excellent mechanical and thermal properties of the S-GF. More importantly, this strategy is scalable. In Figure 3H, a thorough analysis of the variation in thermal performance of M-GFs in response to compression reveals that the range of thermal resistance adjustment during the transition from the off to the on state within the strain range is significantly broadened as the number of stacked layers increases. Within the strain range, the heat transfer capability of S-GF undergoes a substantial reduction, decreasing from 83.83 to 2.67 $cm^2\ K\ W^{-1}$. In contrast, the heat transfer capability of 7-layer GFs exhibits an even more pronounced decline, drastically dropping from 604.85 to 15.49 $cm^2\ K\ W^{-1}$ (Table S4). This characteristic enables these materials to offer versatile tunability across an extremely wide range of heat transfer capabilities. The performance of M-GFs with other macroscopic thermal switch materials[30,31,45–48] were further compared. Figure 3I and Table S5 show that both S-GF and M-GFs exhibit higher SRs. Additionally, the 7-layer GFs demonstrated an even broader range of thermal resistance adjustment, with an SR as high as 39.0. Moreover, this range could achieve an even higher upper limit as the number of stacked layers increased. The M-GFs exhibit an impressive broad range of adjustments, enabling the simultaneous qualification of both thermal insulation and heat dissipation in thermal management systems. This characteristic of significant thermal variation with mechanical stimuli validates the enormous potential of this material in the field of dynamic thermal management.

Heat dissipation and thermal insulation of GF

In most scenarios, effective thermal management of electronic devices necessitates a balance between low-temperature insulation and high-temperature heat dissipation to prevent performance degradation. To this end, we harness the notable heat transfer characteristics of S-GF, which vary significantly with compression levels, to devise an intelligent thermal switch mechanism. Figure 4A demonstrates the application of this thermal switch in a simulated scenario of heat dissipation for electronic components, where S-GF is positioned between the heat source and heat sink, accompanied by a water-cooling system to maintain the heat sink at room temperature. By modulating the compression degree of S-GF, the dynamic changes in the surface temperature of the heat source were recorded, as shown in Figure 4B. Subjected to a constant heating power of 30 W and five cycles of heating-cooling (120 s), the T_{heater} dropped from 151°C to 39°C upon compressing S-GF from its uncompressed state to an 80% compressed state, exhibiting high continuous controllability. This result indicates enhanced thermal conductivity during compression, accelerating heat transfer and effectively lowering the heat source temperature. To explore the potential of S-GF as a thermal interface material (TIM), its heat dissipation performance was further compared at 80% compression with a commercial thermal pad. By placing S-GF between the ceramic heater and the heat sink, as illustrated in Figure 4A, and maintaining a constant heating power of 30 W, the temperature of S-GF was found to be stabilized at 39°C. This represented decreases of 15°C and 8°C, respectively, compared to the cases without TIM and with the commercial thermal pad (Figure 4C), highlighting the exceptional

Please cite this article in press as: Cao et al., Weldable graphene foams for wide-range thermal switches, Cell Reports Physical Science (2025), https://doi.org/10.1016/j.xcrp.2025.102599

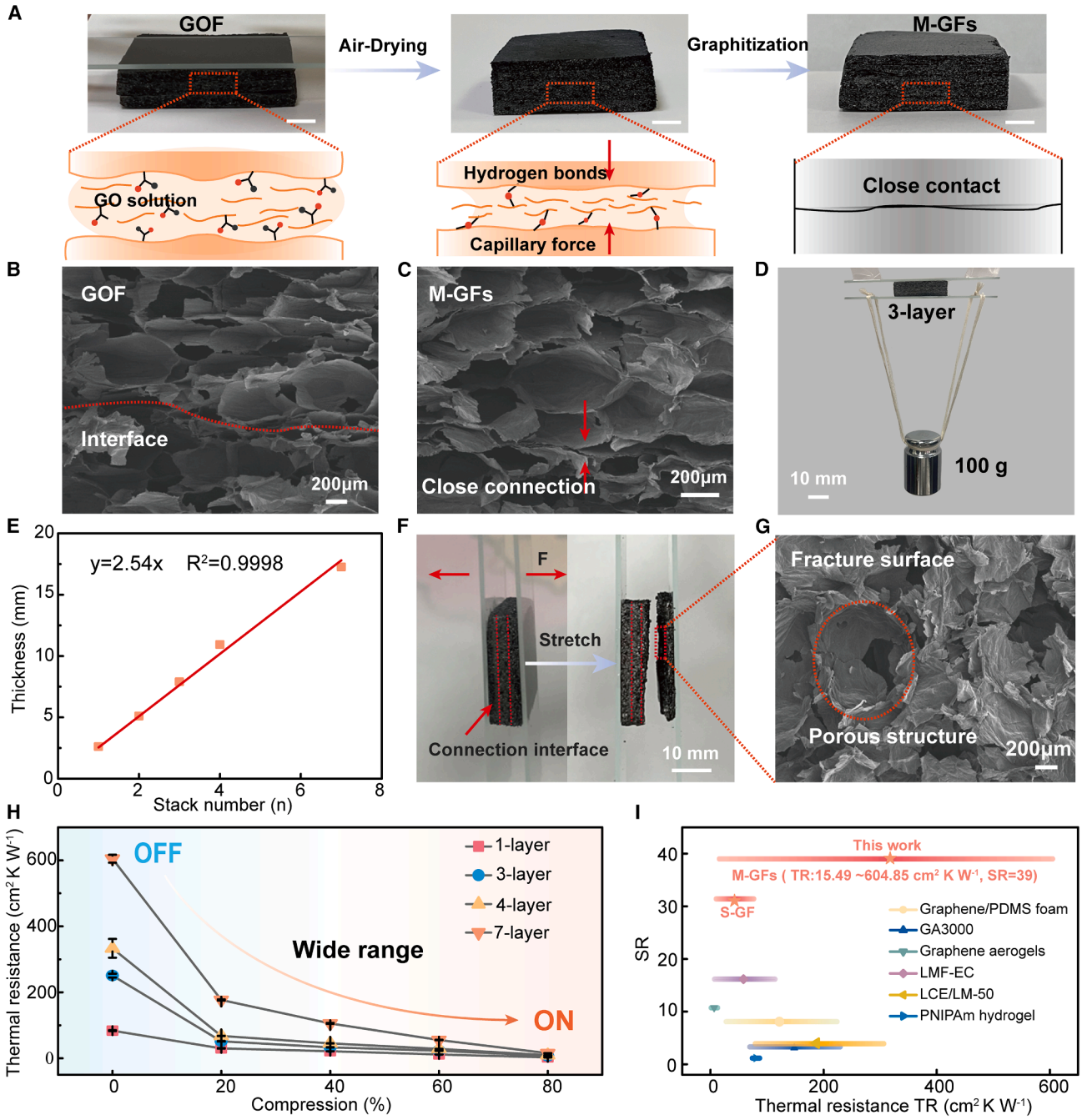

Figure 3. Assembly strategy and thermal switching performance of M-GFs

(A) Assembly process of a monolayer of GOF through GO aqueous solution after air drying and the schematic diagram of dense interface formation process caused by capillary force, hydrogen bonds, and graphitization. The scale bar represents 5 mm.

(B) SEM image of the interface of assembled GOF.

(C) SEM image of the interface of M-GFs with a compact interface and uniform pore structure after graphitization.

(D) Photograph showing 3-layer GFs (≈133 mg) resisting 100 g weight tension without fracture. The scale bar represents 10 mm.

(E) The thickness of GF increases linearly with the number of stacked layers.

(F) Photograph showing the tensile failure test of 3-layer GFs stretched by hand. The scale bar represents 10 mm.

(G) SEM image of the fracture surface of 3-layer GFs.

(H) Thermal resistance of the GF with different stack numbers under various compressive strains.

(I) SR-thermal resistance TR comparison.

Please cite this article in press as: Cao et al., Weldable graphene foams for wide-range thermal switches, Cell Reports Physical Science (2025), https://doi.org/10.1016/j.xcrp.2025.102599

CellPress
OPEN ACCESS

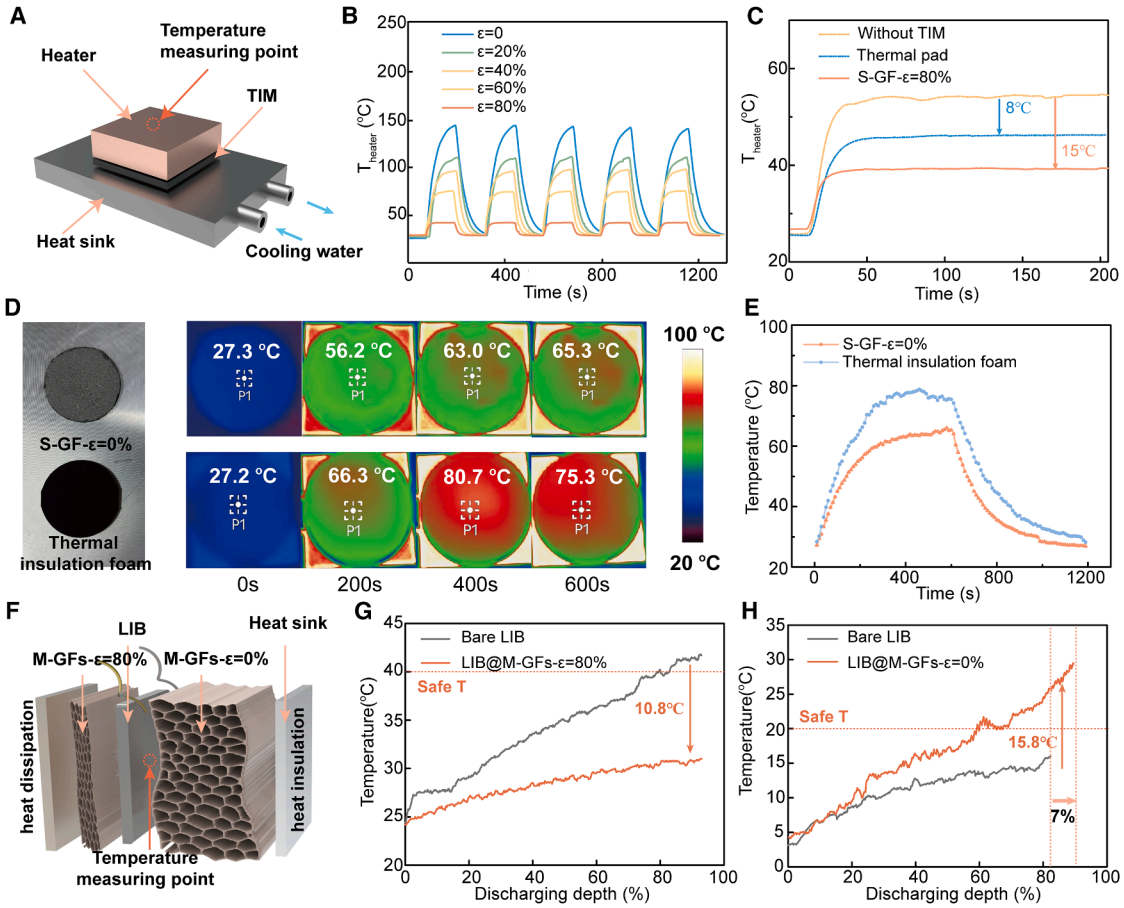

Figure 4. Heat dissipation and insulation applications of GF

(A) Schematic diagram of TIM performance evaluation system.

(B) The surface temperature of the heater under various compressive strains.

(C) Variation of the T_{heater} with heating time at a heating power of 30 W.

(D and E) Infrared images of surface temperature and temperature-time curves of the S-GF and commercial thermal insulation foam at a heating power of 3 W.

(F) Schematic diagram of the experimental setup for thermal management of LIB.

(G and H) Temperature of the battery surface with the discharge depth during the discharge test at various condition.

capability of S-GF in efficient heat conduction. Moreover, to comprehensively evaluate the heat-dissipation performance under various conditions, Figure S22 further compares the T_{heater} of S-GF-ε = 80% and the thermal pad under different heating powers. The S-GF-ε = 80% consistently demonstrates lower T_{heater} and superior heat dissipation capabilities. When S-GF-ε = 80% fully served as a TIM, its thermal resistance was lower than that of the thermal pad under different packaging pressures (Figure S23). Figure S24 demonstrates that S-GF maintains excellent heat dissipation performance even after 500 consecutive heating-cooling cycles, confirming its superior thermal cycling stability under prolonged operation. The thermal insulation of uncompressed S-GF was further compared with that of thermal insulation foam of the same size on a ceramic heater at 3 W (Figures 4D and 4E). The surface temperature of the foam was consistently higher. Moreover, the foam deformed at >80°C, leading to a decrease in temperature between 400 and 600 s, which suggests structural instability at high temperatures and a subsequent impact on its thermal insulation performance. In contrast, S-GF maintained a stable, lower temperature, demonstrating superior insulation. This is vital for maintaining electronic device temperatures to enhance high efficiency and stability under low-temperature environments.

As depicted in Figure 4F, a lithium-ion battery (LIB) thermal management system was established by attaching M-GFs on both sides of the pouch cells for thermal management purposes. The nominal capacity of the pouch cell is 2 Ah. The untreated battery was denoted the bare LIB, the battery with uncompressed M-GFs attached was denoted LIB@M-GFs-ε = 0%, and the battery with 80% compressed M-GFs attached was denoted LIB@M-GFs-ε = 80%. Thermocouples were utilized to monitor the temperature changes during battery discharging. The surface temperature of the battery under different conditions was measured during fast discharging at 4 C. As shown in Figure 4G, the temperature rise of LIB@M-GFs-ε = 80% was significantly slower compared to the bare LIB, decreasing the

temperature from 41.8°C to 31°C at the end of discharge. This result suggests that M-GFs-ε = 80% could reduce the thermal resistance to effectively facilitate heat dissipation. As a high-quality TIM, M-GFs minimized the interfacial thermal resistance between the LIB and the heat sink, enhancing heat dissipation efficiency. Under simulated low-temperature environments (Figure 4H), LIB@M-GFs-ε = 0% exhibited a faster temperature rise compared to the bare LIB, increasing the temperature from 13.7°C to 29.5°C at the end of discharging, producing a 15.8°C increase. It is noteworthy that LIB@M-GFs-ε = 0% maintained a relatively higher capacity, whereas the bare LIB experienced a capacity loss of nearly 7% due to long-term work under such low-temperature conditions. In this scenario, M-GFs-ε = 0% functioned as an insulator, effectively retaining the heat of the battery. Under varying conditions, M-GFs have reached the safe operating temperature for the battery. Figures S25 and S26 compare the performance of M-GFs with those of a commercial thermal pad and insulation foam during 5 charge-discharge cycles at a 4 C rate (CC-CV charging with 4 C-4.25 V-0.4 C and CC discharging with 4 C-2.8 V). M-GFs exhibit superior heat dissipation and insulation capabilities, maintaining consistent temperature profiles throughout the cycles, which confirms their stability and reliability in dynamic thermal management (Note S3). The unique on/off behavior of M-GFs not only underscores their exceptional efficiency as thermal management materials but also highlights their promising potential for applications in dynamic thermal regulation and device thermal protection.

In summary, a scalable assembly strategy utilizing weldable GFs was employed to fabricate a strain-responsive thermal switch with high SRs and a wide TR. S-GF exhibits exceptional elasticity, fatigue resistance, and a range of thermal resistances from 83.83 to 2.67 $cm^2\ K\ W^{-1}$. Benefiting from the effective assembly of GOF, the scalable mechanical and thermal properties enable M-GFs to possess a broader range of thermal resistance from 604.85 to 15.49 $cm^2\ K\ W^{-1}$, achieving an SR of 39.0, which is suitable for dual applications in thermal interface heat transfer and thermal insulation. In the dynamic thermal management of LIBs, M-GFs demonstrate effective thermal performance management under varying conditions, reducing peak temperatures during high-temperature discharge and enhancing discharge capacity and temperature at low temperatures, ensuring the safe temperature range (20°C–40°C) for battery operation. This study provides a scalable strategy for fabricating strain-responsive thermal switches with high SRs and wide adjustment ranges and offers a dynamic thermal management solution for contemporary electronic devices.

METHODS

Further details regarding the methods can be found in the supplemental methods, including the material preparation, detailed characterization, and experimental testing details.

RESOURCE AVAILABILITY

Lead contact

Further information and requests for resources and reagents should be directed to and will be fulfilled by the lead contact, Daping He (hedaping@whut.edu.cn).

Materials availability

This study did not generate new unique reagents.

Data and code availability

- The raw data and images supporting this study are available in the manuscript and its supplemental information or from the lead contact upon request.
- This paper does not report original code.
- Requests for additional information should be addressed to the lead contact.

ACKNOWLEDGMENTS

This work was supported by the National Natural Science Foundation of China (22279097), the Key R&D Program of Hubei Province (2023BAB103), the China Postdoctoral Science Foundation (2024M762511), and the Foundation of National Key Laboratory of Microwave Imaging Technology.

AUTHOR CONTRIBUTIONS

S.C. and H.F. contributed equally to this work. S.C., H.F., L.L., and D.H. conceived and directed the project. S.C. and H.F. wrote the paper. S.C., P. C., C.T., and W.Q. performed the fabrication and characterizations. H.F., Z. Z., and Z.L. helped analyze the data. H.F., L.L., Z.W., and D.H. revised the manuscript and provided suggestions for details in the tests. All authors participated in the discussion of the results, commented on the implications, and fully approved the content of the manuscript.

DECLARATION OF INTERESTS

The authors declare no competing interests.

SUPPLEMENTAL INFORMATION

Supplemental information can be found online at https://doi.org/10.1016/j.xcrp.2025.102599.

Received: February 3, 2025
Revised: March 14, 2025
Accepted: April 18, 2025
Published: May 12, 2025

REFERENCES

1. Moore, A.L., and Shi, L. (2014). Emerging challenges and materials for thermal management of electronics. Mater. Today *17*, 163–174. https://doi.org/10.1016/j.mattod.2014.04.003.
2. Liu, Y., Zhu, Y., and Cui, Y. (2019). Challenges and opportunities towards fast-charging battery materials. Nat. Energy *4*, 540–550. https://doi.org/10.1038/s41560-019-0405-3.
3. Luo, M., Wang, Z., Ke, K., Cao, B., Zhai, Y., and Zhou, X. (2018). Human metabolic rate and thermal comfort in buildings: The problem and challenge. Build. Environ. *131*, 44–52. https://doi.org/10.1016/j.buildenv.2018.01.005.
4. Hu, X., Zheng, Y., Howey, D.A., Perez, H., Foley, A., and Pecht, M. (2020). Battery warm-up methodologies at subzero temperatures for automotive applications: Recent advances and perspectives. Prog. Energ. Combust. *77*, 100806. https://doi.org/10.1016/j.pecs.2019.100806.
5. Liu, T., Hu, X., Li, S.E., and Cao, D. (2017). Reinforcement Learning Optimized Look-Ahead Energy Management of a Parallel Hybrid Electric Vehicle. IEEE/ASME T. Mech. *22*, 1497–1507. https://doi.org/10.1109/TMECH.2017.2707338.
6. Piao, N., Gao, X., Yang, H., Guo, Z., Hu, G., Cheng, H.-M., and Li, F. (2022). Challenges and development of lithium-ion batteries for low temperature

environments. Etransportation *11*, 100145. https://doi.org/10.1016/j.etran.2021.100145.

7. Zhang, S., Shen, Z., and Lu, Y. (2020). Research Progress of Thermal Runaway and Safety for Lithium Metal Batteries. Acta Phys-chim. Sin. *0*, 2008065. https://doi.org/10.3866/PKU.WHXB202008065.
8. Han, Y., Ruan, K., and Gu, J. (2023). Multifunctional Thermally Conductive Composite Films Based on Fungal Tree-like Heterostructured Silver Nanowires@Boron Nitride Nanosheets and Aramid Nanofibers. Angew Chem Int Edit *62*, e202216093. https://doi.org/10.1002/anie.202216093.
9. Tian, C., Fu, H., Wang, Z., Zhang, Z., Qian, W., Zhang, H., Xu, S., Cao, S., and He, D. (2024). Deformable surface design of vertical graphene thermal interface materials for efficient heat dissipation. Cell Rep. Phys. Sci. *5*, 101978. https://doi.org/10.1016/j.xcrp.2024.101978.
10. Fu, H., Fang, R., Tian, C., Qian, W., Cao, S., Zhang, Z., Xu, X., Yao, C., Wang, Z., and He, D. (2024). High-performance thermal interface materials enabled by vertical alignment of lightweight and soft graphene foams. Nano Res. *17*, 9293–9299. https://doi.org/10.1007/s12274-024-6985-7.
11. Hengeveld, D.W., Mathison, M.M., Braun, J.E., Groll, E.A., and Williams, A. D. (2010). Review of Modern Spacecraft Thermal Control Technologies. HVAC R Res. *16*, 189–220. https://doi.org/10.1080/10789669.2010.10390900.
12. Wehmeyer, G., Yabuki, T., Monachon, C., Wu, J., and Dames, C. (2017). Thermal diodes, regulators, and switches: Physical mechanisms and potential applications. Appl. Phys. Rev. *4*, 041304. https://doi.org/10.1063/1.5001072.
13. Ng, B.T., Lim, Z.Y., Hung, Y.M., and Tan, M.K. (2016). Phase change modulated thermal switch and enhanced performance enabled by graphene coating. RSC Adv. *6*, 87159–87168. https://doi.org/10.1039/c6ra17078a.
14. Guo, L., Zhang, X., Huang, Y., Hu, R., and Liu, C. (2017). Thermal characterization of a new differential thermal expansion heat switch for space optical remote sensor. Appl. Therm. Eng. *113*, 1242–1249. https://doi.org/10.1016/j.applthermaleng.2016.11.102.
15. Klinar, K., and Kitanovski, A. (2020). Thermal control elements for caloric energy conversion. Renew. Sustain. Energy Rev. *118*, 109571. https://doi.org/10.1016/j.rser.2019.109571.
16. Lu, Q., Huberman, S., Zhang, H., Song, Q., Wang, J., Vardar, G., Hunt, A., Waluyo, I., Chen, G., and Yildiz, B. (2020). Bi-directional tuning of thermal transport in $SrCoO_x$ with electrochemically induced phase transitions. Nat. Mater. *19*, 655–662. https://doi.org/10.1038/s41563-020-0612-0.
17. Foley, B.M., Wallace, M., Gaskins, J.T., Paisley, E.A., Johnson-Wilke, R.L., Kim, J.-W., Ryan, P.J., Trolier-McKinstry, S., Hopkins, P.E., and Ihlefeld, J. F. (2018). Voltage-Controlled Bistable Thermal Conductivity in Suspended Ferroelectric Thin-Film Membranes. ACS Appl. Mater. Inter. *10*, 25493–25501. https://doi.org/10.1021/acsami.8b04169.
18. Ihlefeld, J.F., Foley, B.M., Scrymgeour, D.A., Michael, J.R., McKenzie, B. B., Medlin, D.L., Wallace, M., Trolier-McKinstry, S., and Hopkins, P.E. (2015). Room-Temperature Voltage Tunable Phonon Thermal Conductivity via Reconfigurable Interfaces in Ferroelectric Thin Films. Nano Lett. *15*, 1791–1795. https://doi.org/10.1021/nl504505t.
19. Yigen, S., and Champagne, A.R. (2014). Wiedemann–Franz Relation and Thermal-Transistor Effect in Suspended Graphene. Nano Lett. *14*, 289–293. https://doi.org/10.1021/nl403967z.
20. Lee, S., Hippalgaonkar, K., Yang, F., Hong, J., Ko, C., Suh, J., Liu, K., Wang, K., Urban, J.J., Zhang, X., et al. (2017). Anomalously low electronic thermal conductivity in metallic vanadium dioxide. Science *355*, 371–374. https://doi.org/10.1126/science.aag0410.
21. Sciortino, F., Mossa, S., Zaccarelli, E., and Tartaglia, P. (2004). Equilibrium Cluster Phases and Low-Density Arrested Disordered States: The Role of Short-Range Attraction and Long-Range Repulsion. Phys. Rev. Lett. *93*, 055701. https://doi.org/10.1103/PhysRevLett.93.055701.
22. Stradner, A., Sedgwick, H., Cardinaux, F., Poon, W.C.K., Egelhaaf, S.U., and Schurtenberger, P. (2004). Equilibrium cluster formation in concentrated protein solutions and colloids. Nature *432*, 492–495. https://doi.org/10.1038/nature03109.
23. Yan, X., Zhao, H., Feng, Y., Qiu, L., Lin, L., Zhang, X., and Ohara, T. (2022). Excellent heat transfer and phase transformation performance of erythritol/graphene composite phase change materials. Compos. Pt. B-Eng. *228*, 109435. https://doi.org/10.1016/j.compositesb.2021.109435.
24. Liu, H., Qin, G., Lin, Y., and Hu, M. (2016). Disparate Strain Dependent Thermal Conductivity of Two-dimensional Penta-Structures. Nano Lett. *16*, 3831–3842. https://doi.org/10.1021/acs.nanolett.6b01311.
25. Qin, G., Qin, Z., Wang, H., and Hu, M. (2018). Lone-pair electrons induced anomalous enhancement of thermal transport in strained planar two-dimensional materials. Nano Energy *50*, 425–430. https://doi.org/10.1016/j.nanoen.2018.05.040.
26. Xie, H., Ouyang, T., Germaneau, É., Qin, G., Hu, M., and Bao, H. (2016). Large tunability of lattice thermal conductivity of monolayer silicene via mechanical strain. Phys. Rev. B *93*, 075404. https://doi.org/10.1103/PhysRevB.93.075404.
27. Liu, X., Li, Y., Sun, X., Tang, W., Deng, G., Liu, Y., Song, Z., Yu, Y., Yu, R., Dai, L., and Shui, J. (2021). Off/on switchable smart electromagnetic interference shielding aerogel. Matter *4*, 1735–1747. https://doi.org/10.1016/j.matt.2021.02.022.
28. Wang, Z.Y., Li, Z.C., Li, B., Shi, A.F., Zhang, L., Zhu, Y.B., Ye, F., and Yu, S. H. (2024). Functional Carbon Springs Enabled Dynamic Tunable Microwave Absorption and Thermal Insulation. Adv. Mater. *36*, 2412605. https://doi.org/10.1002/adma.202412605.
29. Li, M., Yin, B., Gao, C., Guo, J., Zhao, C., Jia, C., and Guo, X. (2023). Graphene: Preparation, tailoring, and modification. Exploration *3*, 20210233. https://doi.org/10.1002/EXP.20210233.
30. Du, T., Xiong, Z., Delgado, L., Liao, W., Peoples, J., Kantharaj, R., Chowdhury, P.R., Marconnet, A., and Ruan, X. (2021). Wide range continuously tunable and fast thermal switching based on compressible graphene composite foams. Nat. Commun. *12*, 4915. https://doi.org/10.1038/s41467-021-25083-8.
31. Cheng, S., Guo, X., Tan, P., Yan, B., Lin, M., Cai, J., Zhang, Y., Cai, W., and Zhang, X.a. (2023). A graphene aerogel with reversibly tunable thermal resistance for battery thermal management. J. Mater. Chem. A *11*, 17779–17786. https://doi.org/10.1039/D3TA03190J.
32. Liu, Y., Qiu, L., Wang, Z., Li, H., and Feng, Y. (2024). Enhancing interfacial thermal transport efficiently in diamond/graphene heterostructure by involving vacancy defects. Compos. Part A: Appl. Sci. Manu. *178*, 108008. https://doi.org/10.1016/j.compositesa.2024.108008.
33. Li, X.H., Liu, P., Li, X., An, F., Min, P., Liao, K.N., and Yu, Z.Z. (2018). Vertically aligned, ultralight and highly compressive all-graphitized graphene aerogels for highly thermally conductive polymer composites. Carbon *140*, 624–633. https://doi.org/10.1016/j.carbon.2018.09.016.
34. Liu, P., Li, X., Min, P., Chang, X., Shu, C., Ding, Y., and Yu, Z.Z. (2020). 3D Lamellar-Structured Graphene Aerogels for Thermal Interface Composites with High Through-Plane Thermal Conductivity and Fracture Toughness. Nano-Micro Lett. *13*, 22. https://doi.org/10.1007/s40820-020-00548-5.
35. Zong, D., Bai, W., Geng, M., Yin, X., Yu, J., Zhang, S., and Ding, B. (2022). Bubble Templated Flexible Ceramic Nanofiber Aerogels with Cascaded Resonant Cavities for High-Temperature Noise Absorption. ACS Nano *16*, 13740–13749. https://doi.org/10.1021/acsnano.2c06011.
36. Yang, H., Jin, X., Sun, G., Li, Z., Gao, J., Lu, B., Shao, C., Zhang, X., Dai, C., Zhang, Z., et al. (2020). Retarding Ostwald Ripening to Directly Cast 3D Porous Graphene Oxide Bulks at Open Ambient Conditions. ACS Nano *14*, 6249–6257. https://doi.org/10.1021/acsnano.0c02379.
37. Qiu, L., Liu, J.Z., Chang, S.L.Y., Wu, Y., and Li, D. (2012). Biomimetic superelastic graphene-based cellular monoliths. Nat. Commun. *3*, 1241. https://doi.org/10.1038/ncomms2251.

38. Si, Y., Wang, X., Dou, L., Yu, J., and Ding, B. (2018). Ultralight and fire-resistant ceramic nanofibrous aerogels with temperature-invariant superelasticity. Sci. Adv. *4*, eaas8925. https://doi.org/10.1126/sciadv.aas8925.

39. Yang, H., Li, Z., Sun, G., Jin, X., Lu, B., Zhang, P., Lin, T., and Qu, L. (2019). Superplastic Air-Dryable Graphene Hydrogels for Wet-Press Assembly of Ultrastrong Superelastic Aerogels with Infinite Macroscale. Adv. Funct. Mater. *29*, 1901917. https://doi.org/10.1002/adfm.201901917.

40. Luo, C., Yeh, C.-N., Baltazar, J.M.L., Tsai, C.-L., and Huang, J. (2018). A Cut-and-Paste Approach to 3D Graphene-Oxide-Based Architectures. Adv. Mater. *30*, 1706229. https://doi.org/10.1002/adma.201706229.

41. Cheng, H., Huang, Y., Cheng, Q., Shi, G., Jiang, L., and Qu, L. (2017). Self-Healing Graphene Oxide Based Functional Architectures Triggered by Moisture. Adv. Funct. Mater. *27*, 1703096. https://doi.org/10.1002/adfm.201703096.

42. Medhekar, N.V., Ramasubramaniam, A., Ruoff, R.S., and Shenoy, V.B. (2010). Hydrogen Bond Networks in Graphene Oxide Composite Paper: Structure and Mechanical Properties. ACS Nano *4*, 2300–2306. https://doi.org/10.1021/nn901934u.

43. Wang, Z., Mao, B., Zhao, M., Calatayud, D.G., Qian, W., Li, P., Hu, Z., Fu, H., Zhao, X., Yan, S., et al. (2022). Ultrafast Macroscopic Assembly of High-Strength Graphene Oxide Membranes by Implanting an Interlaminar Superhydrophilic Aisle. ACS Nano *16*, 3934–3942. https://doi.org/10.1021/acsnano.1c09319.

44. Zhang, X., Guo, Y., Liu, Y., Li, Z., Fang, W., Peng, L., Zhou, J., Xu, Z., and Gao, C. (2020). Ultrathick and highly thermally conductive graphene films by self-fusion strategy. Carbon *167*, 249–255. https://doi.org/10.1016/j.carbon.2020.05.051.

45. Guo, X., Cheng, S., Yan, B., Li, Y., Huang, R., Li, J., Cai, W., Zhang, Y., Zhou, Y., and Zhang, X.A. (2022). Free-standing graphene aerogel with improved through-plane thermal conductivity after being annealed at high temperature. J. Colloid Interface Sci. *608*, 2407–2413. https://doi.org/10.1016/j.jcis.2021.10.134.

46. Yu, D., Liao, Y., Song, Y., Wang, S., Wan, H., Zeng, Y., Yin, T., Yang, W., and He, Z. (2020). A Super-Stretchable Liquid Metal Foamed Elastomer for Tunable Control of Electromagnetic Waves and Thermal Transport. Adv. Sci. *7*, 2000177. https://doi.org/10.1002/advs.202000177.

47. Chen, C., Yu, H., Lai, T., Guo, J., Qin, M., Qu, Z., Feng, Y., and Feng, W. (2023). Flexible and elastic thermal regulator for multimode intelligent temperature control. Susmat *3*, 843–858. https://doi.org/10.1002/sus2.171.

48. Feng, H., Tang, N., An, M., Guo, R., Ma, D., Yu, X., Zang, J., and Yang, N. (2019). Thermally-Responsive Hydrogels Poly(N-Isopropylacrylamide) as the Thermal Switch. J. Phys. Chem. C *124*, 7597. https://doi.org/10.1021/acs.jpcc.0c01867.